AIAA JOURNAL
Vol. 54, No. 3, March 2016

Buzz Cycle Description in an Axisymmetric Mixed-Compression Air Intake

Mohammad Reza Soltani*
Sharif University of Technology, 145888 Tehran, Iran
and
Javad Sepahi-Younsi†
Ferdowsi University of Mashhad, 91779 Mashhad, Iran

DOI: 10.2514/1.J054215

Buzz phenomenon is shock oscillation ahead of the supersonic air intake when its mass flow rate is decreasing at off-design condition. The buzz onset and the buzz cycle of an axisymmetric mixed-compression supersonic intake have been experimentally investigated through pressure recording and shadowgraph flow visualization. The intake was designed for a freestream Mach number of 2.0; however, tests were conducted for $M_\infty = 1.8$, 2.0, and 2.2. All tests were performed at 0 deg angle of attack. Results show that there is a strong relation between the acoustic characteristics of the intake and the buzz fluctuations. This relation causes a new pattern for the buzz oscillations, large-amplitude oscillations with large frequency, that has features of both little buzz (Ferri-type instability) and big buzz (Dailey-type instability). Flow separation caused by the shock-wave/boundary-layer interaction and acoustic compression waves are the most important driving mechanisms in the buzz cycle. Both amplitude and frequency of the buzz oscillations vary as the backpressure is varied. As the freestream Mach number is increased, the dominant frequency of the buzz oscillations is decreased.

Nomenclature

c	=	sound speed, m/s
d	=	model maximum diameter, m
EBR	=	exit blockage ratio, %
f	=	fundamental frequency, Hz
L	=	distance from cowl lip to intake exit, m
l	=	model characteristic length, m
M	=	Mach number
P	=	static pressure, Pa
Re	=	unit Reynolds number, 1/m
t	=	time, s
x	=	axial coordinate, m
Δ	=	difference
ϕ	=	circumferential direction, deg

Subscripts

i	=	inlet of the model
n	=	counter
s	=	static conditions
t	=	total conditions
∞	=	freestream condition

I. Introduction

SUPERSONIC air intake is the major component of a supersonic engine. It should decelerate the incoming supersonic air to a low subsonic flow with a minimum possible total pressure loss. In addition, stable and efficient combustion requires the intake to deliver the demanded amount of flow with a maximum possible uniformity for all flight conditions [1]. However, combustion pressure fluctuations or freestream flow disturbances may result in the shock oscillation ahead of the intake, a phenomenon called buzz [2]. This phenomenon can reduce the engine thrust and may even extinguish combustion [3]. Therefore, recognition and prediction of the flow stability characteristics during the buzz is a critical issue.

Buzz oscillations are self-excited and occur due to flow separation over the intake walls [4]. There are two major criteria that describe buzz onset as well as its characteristics. One is named the Ferri criterion [5], according to which buzz is initiated when the vortex sheet originated from the intersection point of the oblique and normal shocks impinges with the cowl lower surface. This leads to flow separation near the cowl surface and chokes the flow in the subsonic diffuser. Another criterion is called the Dailey [6] criterion, which occurs when the flow separation over the compression surface downstream of the interaction point of the shock wave and the boundary layer chokes the flow at the intake throat and triggers the buzz.

Fisher et al. [7] observed and introduced two forms of oscillations during the buzz and termed them little and big buzz. When the intake mass flow rate is started to decrease, small-amplitude oscillations (little buzz) are first observed. These oscillations are related to the Ferri criterion. However, with further reduction of the mass flow rate, large-amplitude oscillations (big buzz) are encountered that are due to the Dailey criterion. They claimed that the frequencies of little and big buzz are similar; however, further investigations [8] showed that this is not true. In addition, Fisher et al. [7] studied the Ferri criterion and showed that collision of the vortex sheet with the lower surface of the cowl may not always trigger the buzz. They found that if the ratio of the total pressure differences across the vortex sheet to the freestream total pressure exceeds about 7%, the buzz will be initiated.

Newsome [9] attempted to find a link between the buzz phenomenon and the acoustic characteristics of the intake duct based on Hankey and Shang's [4] findings. He considered the intake as a duct with an open and a closed end and proposed the fundamental frequency of acoustic resonance in this duct as the buzz frequency. Trapier et al. [8] showed that this frequency is approximately similar to the little buzz frequency for some cases.

In addition to Newsome [9], other researchers studied analytical modeling of the buzz phenomenon [10–16]. Sterbentz et al. [10,11] considered a ram jet engine as a Helmholtz resonator and found that the buzz starts if the curve of the intake pressure recovery as a function of mass flow rate has a positive slope greater than a critical value. However, Trimpi [12] developed a theory based on the quasi-one-dimensional flow and showed that the resonator analysis of

Received 22 January 2015; revision received 26 August 2015; accepted for publication 27 September 2015; published online 15 December 2015.

*Professor, Department of Aerospace Engineering, P.O. Box 11365-8639; msoltani@sharif.edu.

†Assistant Professor, Department of Mechanical Engineering, Faculty of Engineering, P.O. Box 91775-1111; jsepahi@um.ac.ir.

Sterbentz et al. [10,11] may result in a rough approximation for general trends and for frequency and amplitude of the buzz oscillations. Nagashima et al. [13] solved the wave equation by means of the small-perturbation method in a simple circular duct as the intake to find the buzz frequency. They showed that the one-dimensional model is sufficient to model the buzz phenomenon, especially for its frequency, so long as the freestream Mach number is not near 1.0 and the centerbody diameter of the intake is much smaller than the cowl diameter. Park et al. [15] proposed a low-order model for buzz oscillations that solves lumped-parameter ordinary differential equations in time for mass flow, pressures, and temperatures at specific locations in the engine. However, this model requires combustor efficiency, average temperatures, time lag constants, and other quantities that would be difficult to estimate, and therefore, the results were not very accurate.

As seen, up to now no reliable prediction method of intake buzz has been developed through the analytical investigations. Therefore, numerical [9,17–30] or experimental [8,13,23,25,27,31–44] methods are often used to study the buzz onset as well as its frequency and amplitude for various flow conditions. It seems that the work done by Trapier et al. [18] is the most complete study among the numerical investigations because the flow separation is the key phenomenon in the buzz onset according to the Ferri [5] and Dailey [6] criteria, and to the authors' knowledge, this study is the only numerical investigation that uses the large-eddy simulation approach (detached-eddy simulation turbulence model) and three-dimensional grid to study buzz. As a result, the flow separation and buzz phenomenon were simulated more accurately in this study, and validations done by the authors using their experimental data confirm this subject.

In spite of these observations, no complete satisfactory explanation of the buzz cycle is available in the open literature, and only a concise description can be found in [8]. To fill this existing gap, the buzz cycle of a mixed-compression axisymmetric intake has been described briefly in this study. This description is based on the pressure recordings and shadowgraph pictures of the wind-tunnel tests. The authors hope that the results of the current study together with previous investigations enhance our knowledge of the buzz phenomenon and help us to a better description of the buzz cycle. The intake has been designed for a freestream Mach number of 2.0. However, wind-tunnel tests are conducted for freestream Mach numbers of 1.8, 2.0, and 2.2 and at 0 deg angle of attack. At every test, several blockage ratios were imposed at the intake outlet to further study the design and off-design operating conditions. For every freestream Mach number, the buzz onset is first investigated, and then buzz cycle is described for one blockage ratio. Relevance of the observed buzz frequencies with acoustic resonance frequencies of the intake duct is studied at every freestream Mach number. Effects of the freestream Mach number are also investigated at the end of the paper.

II. Experimental Setup

A. Wind Tunnel

The suction-type wind tunnel used in this experiment has a rectangular test section of 60×60 cm^2. The turbulence intensity measured by the hot wire and other instruments in the test section changes from 0.4 to 1.4% for Reynolds number of 6.37×10^6 to 7×10^7 per meter [44]. The freestream Mach number in the test section is controlled by a variable nozzle and though throttling the engine. Maximum deviation of the flow angle in the test section at 0 deg angle of attack and at a freestream Mach number of 2.0, the design Mach number, is about 0.5 deg. A pitot tube is used to measure the freestream Mach number with a maximum error of 0.8%. The tunnel was calibrated for the ranges of Mach number, and the flow parameters, such as flow uniformity, flow angularity, and turbulence intensity, were measured and were found to be within the acceptable range for this type of wind tunnel [45]. There exist porous bleed holes on the upper and lower walls of the test section that can stabilize and control wind-tunnel shock and other reflected waves. Side-wall windows of the test section have been made from accurately manufactured optical glasses that allow the flow and shock pattern observation by means of schlieren and shadowgraph flow visualization systems. The tunnel is of indraft one; therefore, total pressure and total temperature in the test section are constant, atmospheric [46]. All tests were conducted at three freestream Mach numbers of 1.8, 2.0, and 2.2 and at 0 deg angle of attack.

B. Model

A photo of the intake model used in this investigation is shown in Fig. 1a. It is an axisymmetric mixed-compression intake with a design Mach number of 2.0 and with an l/d of 3.4, where d is the maximum model diameter $d = 100$ mm. The intake has a semicone angle of 16 deg and a cowl lip diameter of 69 mm, and the maximum diameter of the spike is 35 mm. The intake contraction ratio defined as ratio of the initial cross-sectional area of the captured stream tube to the throat area is 1.4, and the first starting Mach number of the intake is about 2.0. The high contraction ratio that results in a small throat area causes the formation of a relatively weak normal shock inside the intake, and consequently the total pressure loss is reduced [46]. The model was installed at the midsection of the wind tunnel using a C-type mechanism as shown in Fig. 1a. The spike tip cone is replaceable to examine effects of the boundary-layer bleed on the intake performance and stability. However, all results in the current study are for tests with a cone without bleed. Performance of the intake with and without the boundary-layer suction has already been studied [46,47].

A conical plug is located at the end of the model to vary the exit area of the intake during the tests. As seen from Fig. 1b, the plug is moved along the intake centerbody using a small dc motor and a ball screw. The intake mass flow rate and its backpressure are controlled through changing the intake exit area. Note that the backpressure determines the normal shock position, and consequently buzz phenomenon can be triggered via this plug.

C. Test Procedure and Location of Sensors

Tests were conducted for freestream Mach numbers of 1.8, 2.0, and 2.2. All tests were carried out at 0 deg angle of attack. At the beginning of each test, the plug was in its most downstream position that resulted in the maximum exit area, supercritical operating condition (normal shock inside the intake downstream of the throat section). The plug was then moved forward, and the exit area was reduced until other operating conditions were obtained. For every freestream Mach number, eight different exit areas were adjusted, and the data for all sensors were simultaneously collected. Shadowgraph flow visualization system was also used for all test cases at the same time. The camera used in this investigation, AOS X-PRI, has a maximum speed of 1000 frames per second with image dimensions of 800×600 pixels. This speed was sufficient for most test cases investigated in this study.

Forty-two low-frequency and 20 high-frequency pressure transducers have been used for each test to measure static and total pressures on the model and on the wind-tunnel walls. The letters "S" and "T" denote static and total pressure sensors, respectively, in this paper. For every freestream Mach number and for each plug position, the data for all 62 pressure ports were collected simultaneously. All data were acquired at a sampling rate of 2.8 kHz for 1.8 s. Low-frequency sensors were used for steady measurements and for calculation of the performance parameters of the intake such as the total pressure recovery, mass flow ratio, and static distortion [46,47]. These sensors were relatively large and could not be placed inside the model. In addition, their maximum sampling rate was relatively low, about 0.1 kHz; therefore, they were installed outside of the test section and were used for steady measurement cases. However, the high-frequency miniature transducers were used for unsteady measurements and for investigation of the buzz phenomenon because these sensors were very small, about 2.0 millimeters in diameter, and were installed inside the model at a position with the shortest distance from the pressure taps and probes. In addition, their maximum frequency (natural frequency) was very high, about 150 kHz. These sensors are time-accurate differential-type pressure transducers with a maximum combined nonlinearity, hysteresis and repeatability of

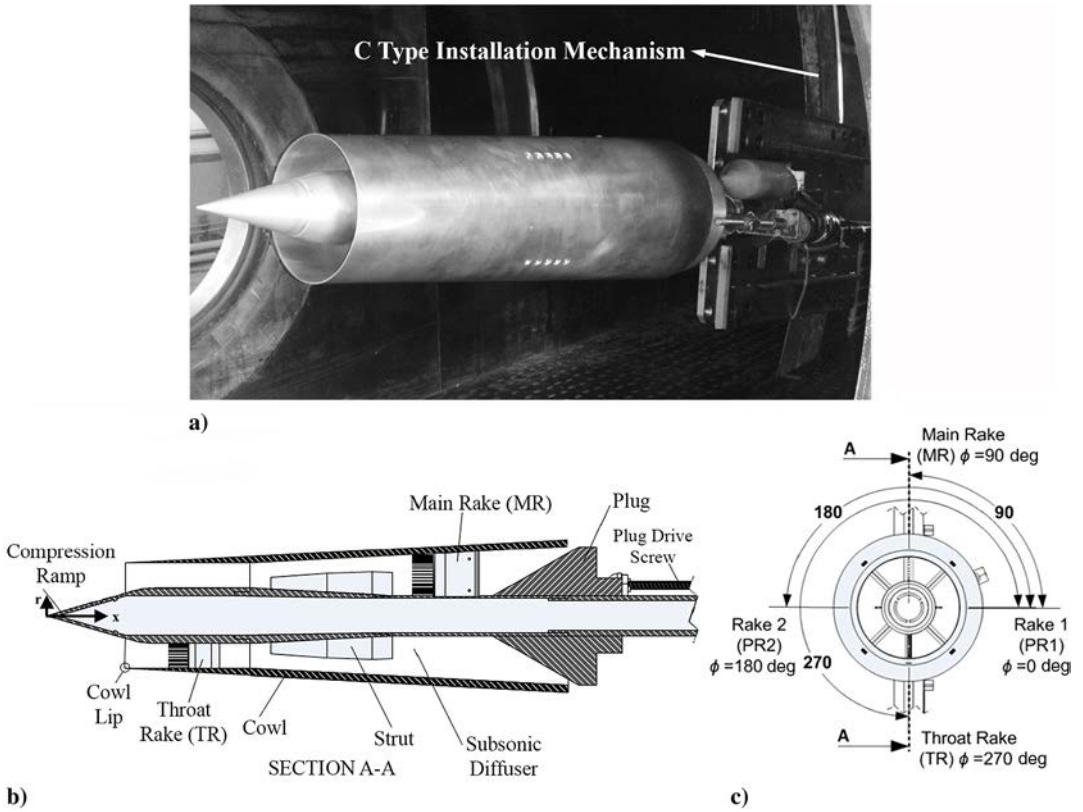

Fig. 1 Details of the intake model and its instruments: a) model in the wind tunnel, b) front view of the model, and c) side view of the model.

$\pm 0.5\%$ of their full-scale output. The pressure range for these transducers is 34, 68, or 102 kPa.

Several pressure taps were drilled at different positions of the spike surface to measure the static pressure distribution. The axial location of these taps will be shown later in the graphs of the spike static pressure distribution. Two multiprobe rakes, the throat rake (TR) and main rake (MR), as shown schematically in Fig. 1c, were located at the throat ($x/d = 0.8$ and $\phi = 270$ deg) and at the exit ($x/d = 2.4$ and $\phi = 90$ deg) sections of the intake. The TR has 12 probes and was used to measure the boundary-layer profile at the throat section. The MR has 17 probes and was used to measure the boundary-layer profile, intake total pressure recovery, mass flow rate, and flow distortion at the exit face of the model. The probe diameter and distance between the probes for the TR are 0.9 and 2.0 mm, respectively, whereas for the MR they were 1.0 and 2.0 mm. As seen from Fig. 1c, two other single-probe rakes (PR1 and PR2) were located at $x/d = 1.4 - \phi = 0$ deg and at $x/d = 1.8 - \phi = 180$ deg, respectively, to measure the total pressure losses of the intake.

The exit blockage ratio (EBR) is used to include effects of the plug movement (exit area variation). This parameter is defined as the ratio of the exit duct height blocked by the plug to the total height of the exit duct. Thus, when EBR is 100%, this means that the exit area of the intake is completely closed, and when it is 0%, it means that the exit area is completely open. The values of EBR used for each freestream Mach number and the corresponding exit area blockage ratios (EABRs) are shown in Table 1. EABR is defined as the exit area blocked by the plug to the total exit area of the intake.

The uncertainties of the measured quantities are given in Table 2. Two values have been reported for the static and total pressure because two different types of pressure transducers were used in this investigation.

Table 1 Values of EBR tested in this experiment and corresponding values of EABR

EBR, %	EABR, %
55.0	42.0
60.0	47.5
62.5	50.3
65.0	53.3
67.5	56.2
70.0	59.3
75.0	66.1
80.0	72.9

III. Results and Discussions

The results are given separately for every freestream Mach number, and the effects of Mach number are studied at the end of the paper. For each freestream Mach number, the buzz onset is investigated first, and then the buzz cycle at one EBR is explained. At the buzz onset section, the pressure signals of some sensors for all EBRs are given to compare the pressure magnitude and fluctuations and to recognize the approximate location of the normal shock, from which the intake operating condition can be revealed. Starting from the smallest EBR, the shadowgraph pictures and power spectral density (PSD) of some pressure signals for every EBR are then investigated to detect the first EBR that the buzz is initiated. The buzz frequency detected from the PSD graphs and the relations obtained between the observed and acoustic resonance frequencies for those

Table 2 Measurement inaccuracies (%) [46,47]

Parameter	Values		
$\Delta P_s/P_s$	0.929, 1.421		
$\Delta P_t/P_t$	0.929, 1.421		
$\Delta P_{s\infty}/P_{s\infty}$	0.012		
$\Delta T_{s\infty}/T_{s\infty}$	0.033		
	$M_\infty = 1.8$	$M_\infty = 2.0$	$M_\infty = 2.2$
$\Delta(Re)/Re$	1.982	1.936	1.791
$\Delta M_\infty/M_\infty$	1.458	1.162	0.918

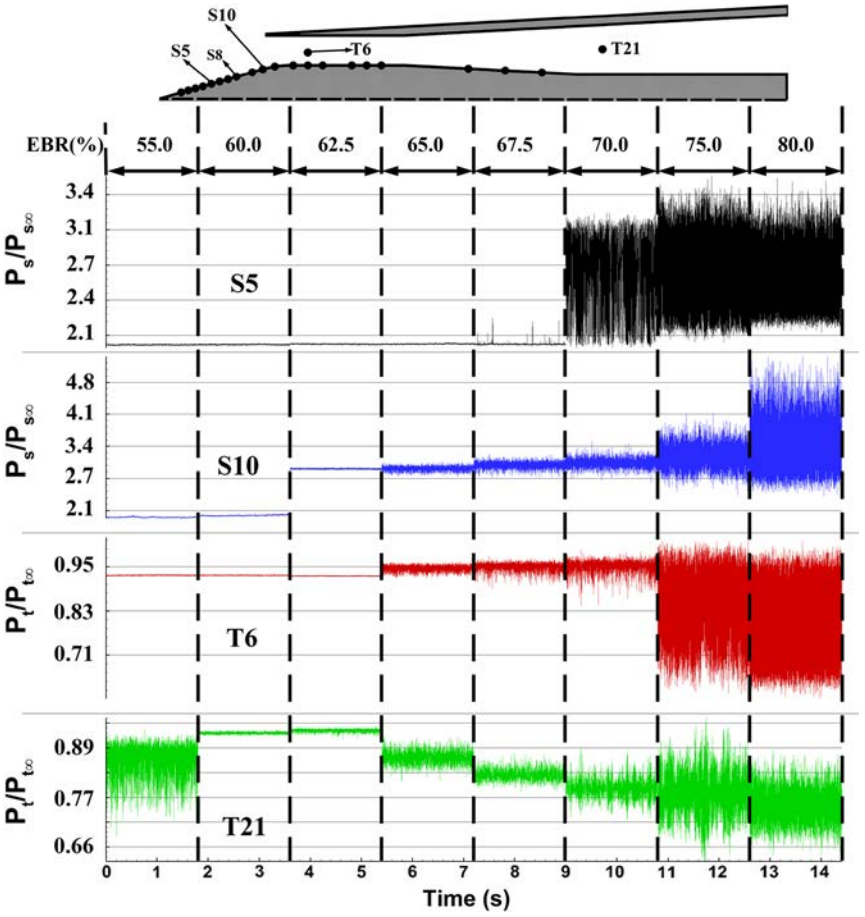

Fig. 2 Pressure recordings of sensors S5, S10, T6, and T21 for $M\infty = 1.8$.

EBRs with buzz are explained in the buzz onset section. At the buzz cycle sections, the buzz cycle for EBR = 80.0% and for EBR = 70.0% is explained for $M_\infty = 1.8$ and $M_\infty = 2.0$, respectively.

A. Buzz Onset for M_∞ Equal to 1.8

Pressure signals of several sensors for $M_\infty = 1.8$ and for all EBRs examined in this study are illustrated in Fig. 2. As mentioned previously in the description of the test procedure, after setting each EBR via a plug through the dc motor, the data for all transducers were acquired simultaneously for 1.8 s. The plug was then moved for the next EBR, and the data were again acquired. Therefore, juxtaposing of the pressure signals for various EBRs as seen in Fig. 2 and in similar figures in this paper does not mean that data for all EBRs were acquired continuously, 14.4 s. All sensors that are named in the intake shown at the top of Fig. 2 (S5 . . . T21) are of high-frequency and high-accuracy transducers that measure either static pressure or total pressure.

As seen from Fig. 2, sensor T21 at EBR = 55.0% has some fluctuations, whereas other sensors do not show fluctuation for this EBR. These oscillations are not related to the buzz phenomenon because, during the buzz, the entire intake flowfield fluctuates. Signal processing including spectrogram for sensor T21 shows that these fluctuations are due to the shock flipping phenomenon that will not be discussed in this paper [1].

Figure 2 shows that there is a pressure jump for sensor S5 when EBR increases from 67.5 to 70%. The reason for this jump is movement of the normal shock to a location upstream of this sensor when EBR is increased. When EBR increases from 60.0 to 62.5%, the normal shock is expelled from the intake, and therefore, subcritical operating condition (normal shock upstream of the throat section) is initiated. This is seen from the pressure jump of the S10 sensor.

Investigation of the shadowgraph pictures shows that, when EBR increases, the first shock oscillation occurs for EBR = 65.0%. However, pressure signal spectra of various sensors do not show any

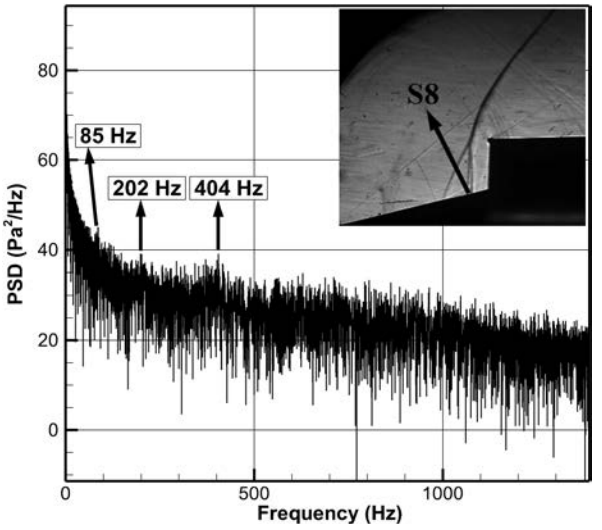

Fig. 3 Spectrum of pressure signal measured by sensor S8 for $M_\infty = 1.8$ and EBR = 65.0%.

dominant frequency, except for sensor S8, which is located just in the vicinity of the shock oscillation, as seen from Fig. 3. All of the PSD graphs presented in this figure and in other similar figures in this paper are in decibels [PSD in dB = $10^* \log_{10}$ (PSD)]. This local shock oscillation is not related to the buzz phenomenon because, as stated in the Ferri and Dailey criteria, the entire intake flowfield must oscillate during the buzz. The local shock oscillation before the buzz onset has been observed also in a two-dimensional (2-D) mixed-compression intake for $M_\infty = 1.8$ [8]. The reason for the lack of obvious frequency in the spectra of the sensor S8 is small energy of

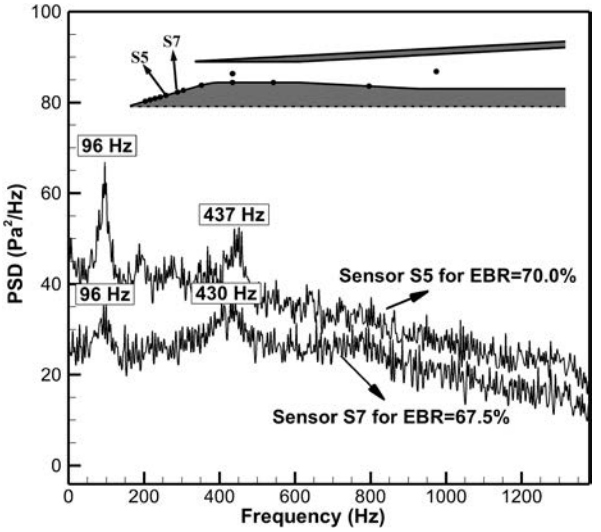

Fig. 4 Spectra of sensors S5 and S7 for $M_\infty = 1.8$.

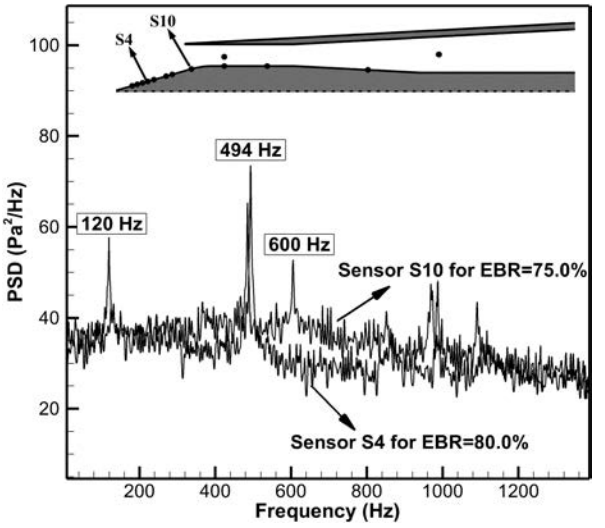

Fig. 5 Spectra of sensors S4 and S10 for $M\infty = 1.8$.

oscillations and viscous damping effects of the wall boundary layer near this pressure tap. All pressure signal spectra presented in this study are single acquisition, and they are not averaged.

For EBR = 67.5%, oscillation of shocks with larger amplitude is seen from the shadowgraph movies. In this case, the dominant frequencies of 96 and 430 Hz are detected from the spectra of few sensors as depicted in Fig. 4. Again, these oscillations are not buzz; however, fluctuations are growing until they encompass the entire intake, and the buzz phenomenon will be initiated. For EBR = 70.0%, spectra of all sensors detect frequencies of 96 and 437 Hz for the buzz oscillations as seen from Fig. 4 for sensor S5. The amplitude of oscillations is larger than that of the previous EBRs.

As mentioned before, Newsome [9] proposed fundamental frequency of the acoustic resonance in the intake duct as the buzz frequency:

$$f_n = (2n+1)\frac{c}{4L}(1-M^2); \qquad n = 0, 1, 2, \ldots \tag{1}$$

L is the distance from the cowl lip to the intake exit over the plug where the flow is choked, and c and M are mean values of sound speed and Mach number inside the intake and are computed from the data of single-probe, main, and throat rakes. These frequencies are presented for $M_\infty = 1.8$ in Table 3. As seen, before the buzz onset for EBR = 65.0 and 67.5%, the resonance frequency for $n = 1$ is approximately equal to the observed frequency (404 Hz for EBR = 65.0%, Fig. 3, and 430 Hz for EBR = 67.5%, Fig. 4). Also, when the buzz is started at EBR = 70.0%, the resonance frequency for $n = 1$ is approximately equal to the observed frequency (437 Hz). Thus, it can be concluded that there are local oscillations due to the acoustic resonance before the buzz onset and after the buzz is started; they are still present, and the buzz is strongly related to the acoustic characteristics of the intake in these conditions. In addition, equal frequencies for oscillations of EBRs 67.5% (before the buzz initiation) and 70.0% (with buzz) reveals that the buzz oscillations are present in the flowfield, and they are amplified with the same frequency when the buzz is started. This issue has already been observed in a 2-D intake [8].

Spectra of the pressure records for EBR = 75% and EBR = 80.0% shows that the buzz frequency is 120 and 494 Hz, respectively, as seen from Fig. 5. Shadowgraph pictures reveals that the buzz amplitude is small for EBR = 70%, and it becomes quite large for EBR = 75% and EBR = 80.0% insofar as the normal shock reaches the spike tip for EBR = 80.0% for some instances of the buzz cycle. Little and big buzz are characterized by their small- and large-amplitude oscillations [7]. In addition, little buzz has higher frequency, which is related to the acoustic resonance [8]. Therefore, the buzz for EBR = 70.0% at $M_\infty = 1.8$ is the little buzz due to the small-amplitude oscillations and its strong relevance to the acoustic resonance. In addition, the oscillations for EBR = 75% and EBR = 80.0% are categorized as the big buzz; however, it is seen that the frequency of the big buzz is large. Buzz with large amplitude and large frequency and novel forms of oscillations have already been observed in [43,35], and the results of the current study confirm them, too.

As seen from Table 3, the observed frequency of big buzz for EBR = 80.0% (494 Hz) is equal to the resonance frequency for $n = 1$. Thus, big buzz for EBR = 80.0% that is related to the Dailey criterion has also characteristics of the little buzz that are due to the Ferri criterion. The reason for this condition may be due to the large separation behind the normal shock (Dailey criterion) and collision of the shear layer resulted from this separation with the inside wall of the cowl that triggers the Ferri criterion. The details of the buzz cycle in this case will be described in the next section.

B. Buzz Cycle for M_∞ Equal to 1.8

The buzz cycle for EBR = 80.0% is described in this section. As seen from Fig. 6, time lapse between t_1 and t_3 indicates period of the buzz cycle. At t_1, sensor S1 has its minimum pressure during the buzz cycle. This condition occurs when the normal shock stands in its most downstream position during the buzz cycle. Shadowgraph pictures show the spatial domain of the buzz oscillations, with one of them shown at the top part of Fig. 7. Using this information, the schematic view of the intake flowfield at t_1 is illustrated in Fig. 7 (bottom part). The horizontal arrow attached to the normal shock shows the direction of movement of this shock in this figure and similarly in

Table 3 Acoustic resonance frequencies for $M_\infty = 1.8$

n	f_n, Hz				
	EBR = 65.0%	EBR = 67.5%	EBR = 70%	EBR = 75%	EBR = 80%
0	115.8	131.6	139.7	155.4	164.4
1	347.4	394.8	419.1	466.3	493.3
2	579.0	658.0	698.4	777.2	822.1
3	810.6	921.2	977.8	1088.1	1150.9

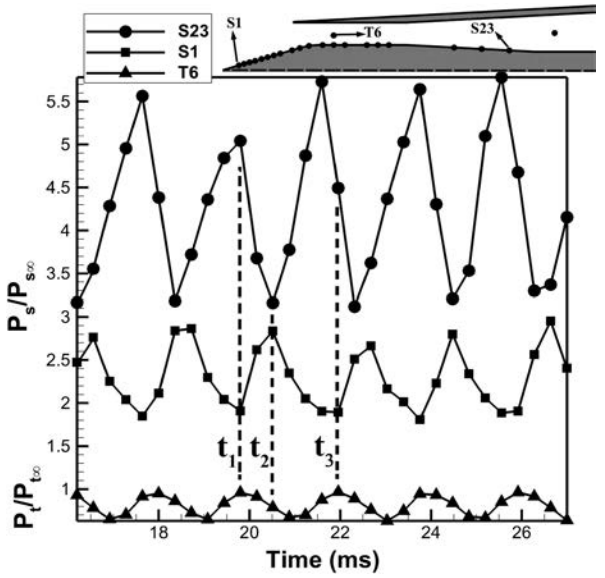

Fig. 6 Time variation of pressure measured by sensors S1, T6, and S23 for $M\infty = 1.8$ and EBR = 80.0% in several cycles of the buzz.

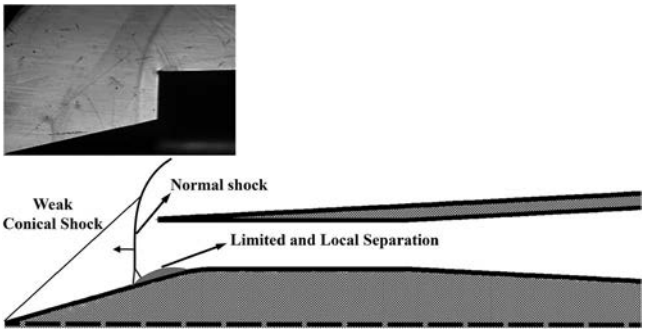

Fig. 7 Shadowgraph picture and approximate schematic view of the flow at t_1.

other figures. In this case, at time t_1, the normal shock is in a position that has the shortest distance to the throat section during the buzz cycle. Therefore, it has its minimum strength relative to other cases, other values of t, and as seen from Fig. 6, the total pressure of sensor T6 is maximum at t_1. Note that transducer T6 measures total pressure. The separation region behind the normal shock is local and has limited effects in this case, time t_1. In addition, both the intake mass flow rate and consequently the intake pressure measured by sensor S23 in Fig. 6 are maximum for this condition.

High-pressure flow inside the intake causes the normal shock to move forward from time t_1 to t_2. According to the Dailey criterion, the separation region and the flow spillage around the cowl lip increase when the normal shock moves upstream. The intake mass flow rate reduces, and according to Fig. 6, the static pressure of sensor S23 and the total pressure of sensor T6 both decrease from time t_1 to t_2.

When $t = t_2$, as seen from Fig. 8, the normal shock reaches its most upstream location during a cycle of the buzz, and it coincides with the conical shock and its strength increases. Because of the large flow separation behind the tip shock wave and large flow spillage in this condition, the intake mass flow rate becomes minimum, and according to Fig. 6, the static pressure inside the intake, S23, reaches its minimum value. As mentioned before, collision of the shear layer of the separation region with the cowl surface triggers the Ferri-type instabilities. Large flow separation in such a way that covers the entire intake flowfield during a short time of the buzz cycle has already been observed numerically [30] and experimentally [34]. In this condition, the overall direction of the flow inside the intake may be reversed for a short time. However, when the normal shock moves downstream and

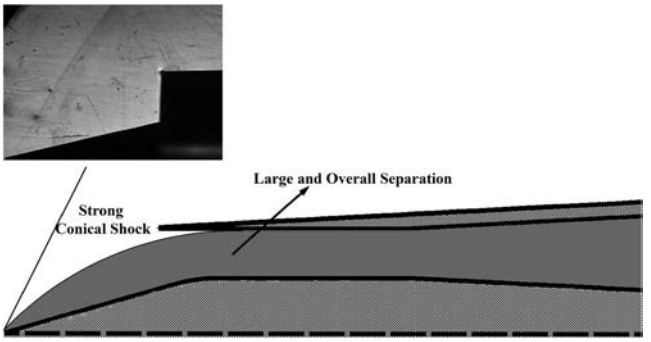

Fig. 8 Shadowgraph picture and approximate schematic view of the flow at t_2.

the flow separation region is reduced, the aforementioned condition is eliminated.

Small mass flow rate and low static pressure inside the intake lead to swallowing of the separated flow inside the intake and move the shock toward the intake entrance during time interval of t_2 to t_3. The normal shock is weakened, and the intake mass flow rate increases during this period, and as seen from Fig. 6, the static pressure of sensor S23 and the total pressure of the sensor T6 both increase. At $t = t_3$, the normal shock reaches probably a position that is very close to its previous location at $t = t_1$ because, at this time, as seen from Fig. 6, the total pressure measured by sensor T6 and the static pressure measured by sensor S1 both reach again their maximum and minimum values, respectively. Therefore, the overall flowfield at $t = t_3$ is again like that one illustrated in Fig. 7 for $t = t_1$. At $t = t_3$ the intake mass flow rate and the static pressure obtained from sensor S23 are approximately maximum again, which causes the normal shock to move upstream, and one cycle of the buzz is then completed.

C. Buzz Onset for M_∞ Equal to 2.0

The pressure signals of several sensors for $M_\infty = 2.0$ and for various EBRs are depicted in Fig. 9. Similar to $M_\infty = 1.8$, for EBR = 62.5%, the intake operating condition becomes subcritical because of the jump in the static pressure measured by the sensor S10 located in the intake entrance, as seen from the top portion of Fig. 9. Shadowgraph pictures and spectra of the various sensors do not reveal any oscillation for EBR = 62.5%. Spectra of the various sensors also do not show any dominant frequency for EBR = 65.0%. However, similar to $M_\infty = 1.8$, shadowgraph pictures show local fluctuations for this EBR that are dissipated in the surface boundary layer, and the pressure sensors are not able to detect them.

When EBR increases to 67.5%, relatively large fluctuations are seen from pressure signals of sensors S5, S10, and T21, which are shown in Fig. 9. Further, from the shadowgraph movies, it is observed that the buzz has been started, and shock waves fluctuate with a large amplitude, and in some instances, the normal shock enters the intake, too; however, as seen from Fig. 9, the normal shock does not reach the position of sensor S1 at all. The spectrum of the pressure signal of sensor S10 (Fig. 10) reveals that the dominant frequency of the buzz phenomenon is about 90.0 Hz for this condition. The buzz frequencies for EBR = 70.0, 75.0, and 80.0% are 96, 113, and 127 Hz, respectively, as seen from Fig. 11. Using this figure and the shadowgraph pictures, it is found that both frequency and amplitude of the buzz oscillations increase when EBR increases. Higher EBR results in a larger backpressure and forces the normal shock to move farther upstream. Thus, according to the Dailey criterion, a larger separation region is formed, and the conditions for triggering the buzz oscillations is met in a shorter time.

When EBR increases from 65.0 to 67.5%, the buzz fluctuations suddenly start with a large amplitude. Therefore, it seems that the present intake does not have little buzz at $M_\infty = 2.0$, at least for discrete EBRs tested in this experiment. A shadowgraph picture of the flowfield ahead of the intake for EBR = 65.0%, the last stable EBR before the buzz onset, is shown in Fig. 12. As seen from this figure, the intersection point of the conical shock originated from the

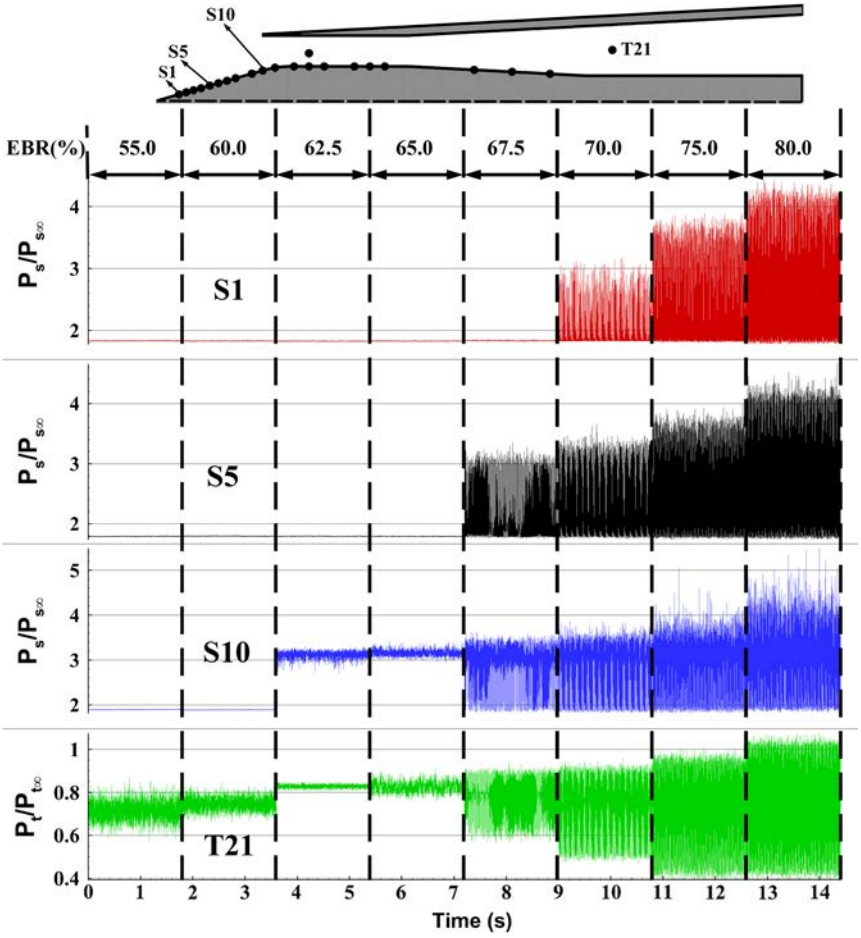

Fig. 9 Pressure recordings measured by sensors S1, S5, S10, and T21 for $M_\infty = 2.0$.

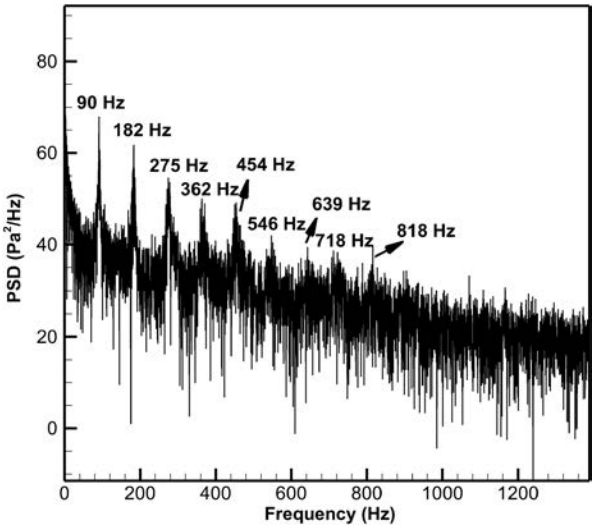

Fig. 10 Spectrum of pressure signal measured by sensor S10 for $M_\infty = 2.0$ and EBR = 67.5%.

tip of the spike, and the normal shock, point A shown in Fig. 12, lies above the cowl lip, and the resulting vortex sheet cannot collide with the internal surface of the cowl to trigger little buzz according to the Ferri criterion. Figure 12 also shows a secondary conical shock after the tip shock wave that is generated due to the presence of a very small step in the junction point of the first and the second parts of the spike as shown in Fig. 1. The vortex sheet that is originated from the intersection point of this shock wave with the normal shock wave may impinge at the interior surface of the cowl. However, this shock is very weak, and the resulting vortex sheet does not have enough strength to trigger the buzz onset. As mentioned before, the ratio of the total pressure differences across the vortex sheet to the freestream total pressure should exceed 7% to trigger the little buzz [7].

Both the calculated resonance and the observed frequency for the buzz oscillations are shown in Table 4 for $M_\infty = 2.0$. As seen, for EBR = 75.0% and EBR = 80.0%, the buzz frequency is approximately equal to the frequency of the first mode, $n = 0$, of the acoustic resonance. Similar to $M_\infty = 1.8$, the reason may be due to the collision of the separation shear layer region with the internal surface of the cowl that can trigger the Ferri-type instabilities in addition to the Dailey-type ones.

D. Buzz Cycle for M_∞ Equal to 2.0

The buzz cycle for EBR = 70.0% is described in this section. Time variation of three static pressure sensors (S1, the most upstream sensor; S10, located at the intake entrance; and S23, located in the subsonic diffuser) together with a buzz cycle period from 49.2 to 59.7 ms is shown in Fig. 13. Shadowgraph pictures for this EBR show that the normal shock lies inside the intake for some instances of the buzz cycle, and as a result, the buzz cycle includes subcritical and supercritical operating conditions that are shown in Fig. 13. To find the edge of these conditions, variation of the Mach number at the intake throat is shown in Fig. 14. As seen from this figure, from $t \approx 57.5$ ms to the end of the buzz cycle, the flow at the intake throat is supersonic. Supersonic flow at the throat section implies the presence of a normal shock in the subsonic diffuser that results in the supercritical operating condition.

At $t \approx 50.0$ ms, the internal normal shock is expelled out from the intake due to the high EBR and moves toward the spike tip. As seen from Fig. 13, sensor S10 has a pressure jump at this time, and the static pressure obtained from sensor S1, located upstream of the normal shock, is minimum. Because of the small distance between the normal shock and the intake throat section at $t = 50.0$ ms, the

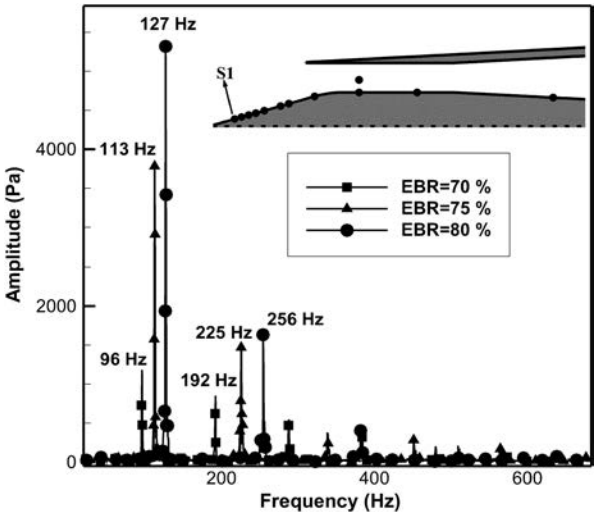

Fig. 11 Spectra of pressure signals measured by sensor S1 for $M_\infty = 2.0$ and EBR = 70.0, 75.0, and 80.0%.

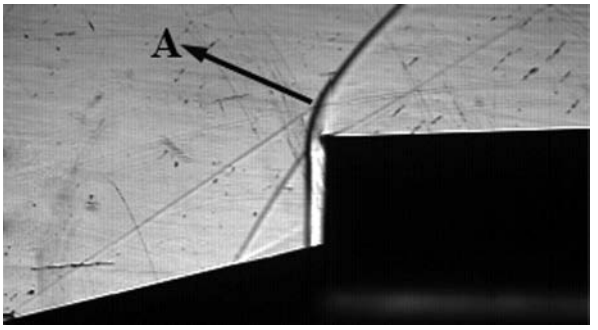

Fig. 12 Shadowgraph picture for $M_\infty = 2.0$ and EBR = 65.0%.

flow spillage is small, and consequently the intake has a large mass flow rate, and the static pressure inside the intake is relatively large; see the output of sensor S23 for $t = 50.0$ ms, shown in Fig. 13.

Flow characteristics including shadowgraph picture, schematic view, and instantaneous pressure distribution over the spike are illustrated for $t \approx 50.0$ ms in Fig. 15. Spike pressure distribution has been obtained from the high-frequency transducers. The pressure jump from sensor S8 to sensor S10 shown in Fig. 15 indicates that the normal shock is placed at the intake entrance at this time $t \approx 50.0$ ms. This can be seen from the shadowgraph picture shown at the top of Fig. 15 and is shown in schematic view of Fig. 15. The normal shock is weak for this case, and as a result, no considerable separation takes place inside the intake. It should be mentioned that the data acquisition as well as recording of the shadowgraph pictures were not synchronized. The shadowgraph picture corresponding to $t \approx 50.0$ ms has been obtained from the pictures of one cycle of the buzz for EBR = 70.0%.

According to the Dailey criterion, when the normal shock moves upstream, the separation increases, and as a result, the intake mass flow rate decreases. At $t = 52.0$ ms, as seen from Fig. 13, the static pressure inside the intake, output of sensor S23, starts to decrease; however, the shock waves have not reached sensor S1 yet, and this sensor shows a constant pressure at this time. Flow characteristics for $t \approx 52.0$ ms are shown in Fig. 16. A lambda shock wave has been generated due to the interaction of the normal shock with the boundary layer, and one of its legs impinges between sensor S2 and sensor S3. In spite of the large flow separation, sensor T6 is out of this region, and Fig. 14 shows that the Mach number is about 0.56 at this time. Local fluctuations of the static pressure of sensor S10 at this time and for other instances around $t = 52.0$ ms (Fig. 13) are due to the fluctuations inside the separation region. The separation zone shown in the schematic view of Fig. 16 and in other similar figures in this paper is the approximate region of separation that do not violate the data of high-frequency pressure transducers. Spike pressure distribution at this time is compared with $t = 50.0$ ms and other times in Fig. 17. This figure also confirms movement of the normal shock toward the spike tip.

At $t = 53.0$ ms, the shock waves reach approximately their most upstream position during a cycle of the buzz, as shown schematically in Fig. 18. Comparing the static pressure measured from sensor S1 at this time $t = 53.0$ ms with the previous time $t = 52.0$ ms, shown in Fig. 17, it is seen that the pressure ratio increases from a value below 1.9 to a value about 2.7. Therefore, it is concluded that this sensor lies downstream of the forward leg of the lambda shock wave, as seen from Fig. 18. The flow separation for this time $t = 53.0$ ms covers a large portion of the intake up to sensor T6. From Fig. 14, it is seen that, for this time, the Mach number at sensor T6 is about 0.08. Large

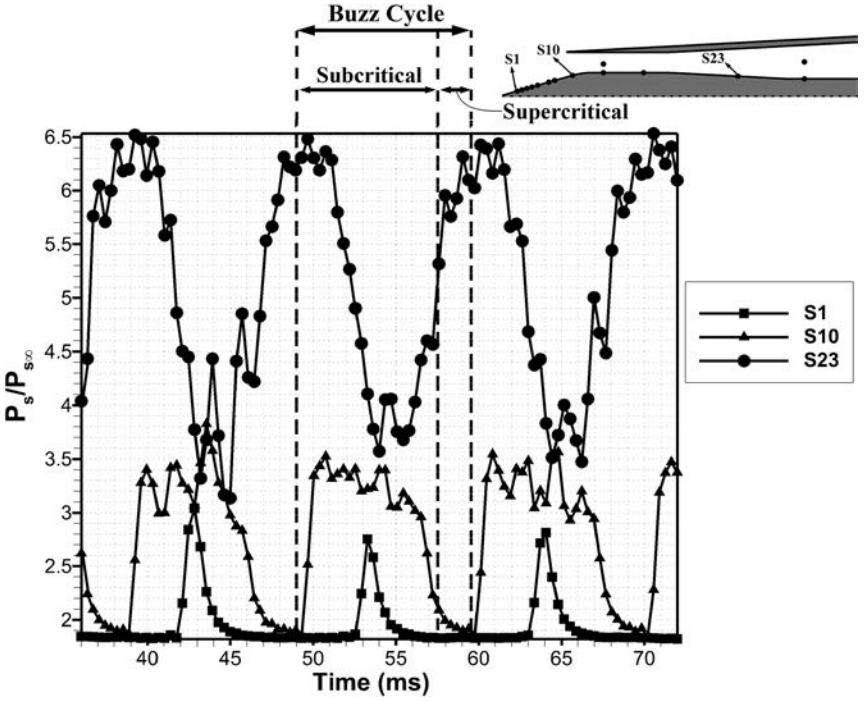

Fig. 13 Static pressure variation measured by sensors S1, S10, and S23 for $M_\infty = 2.0$ and EBR = 70.0%.

Table 4 Acoustic resonance frequencies for $M_\infty = 2.0$

	f_n, Hz			
n	EBR = 67.5%	EBR = 70%	EBR = 75%	EBR = 80%
0	120.3	115.4	116.1	120.7
1	360.8	346.3	348.2	362.2
2	601.4	577.2	580.3	603.7
3	841.9	808.1	812.4	845.2
Observed frequency, Hz	90.0	96.0	113.0	127.0

flow separation also causes the spike pressure distribution to be flattened, as seen from Fig. 17. The static pressure inside the intake, sensor S23, and the Mach number at the intake throat, sensor T6, have approximately their minimum values for $t = 53.0$ ms according to Figs. 13 and 14.

Low values of static pressure inside the intake and downstream of the shock waves cause the separated flow to be swallowed by the intake and the shock waves move downstream, as shown schematically in Fig. 19. The overall configuration of the intake flowfield at $t = 56.0$ ms is similar to that of $t = 52.0$ ms that is shown in Fig. 16. However, the separated region is moved farther down toward the end of the intake at this time $t = 56.0$ ms and causes the spike static pressure distribution to be flatter than the corresponding one for $t = 52.0$ ms, as seen from Fig. 17. Sensor T6 lies out of the separated region, and the value of the Mach number read by this sensor is about 0.57, which is approximately equal to 0.56, its value at $t = 52.0$ ms, as seen from Fig. 14. Because both the separated region and the flow spillage are reduced, the intake mass flow rate and consequently the static pressure of the sensor S23 begins to increase for this time $t = 56.0$ ms, as seen from Fig. 13.

Figure 20 shows time variation of ΔP_s, the static pressure ratio of sensor S23 minus static pressure ratio of sensor S18. From this figure, it is seen that, at $t = 53.0$ ms, the shock waves are approximately at their most upstream position, where ΔP_s is approximately zero. Separation of the flow at this time $t = 53.0$ ms is so large that it covers the entire intake and results in the same pressure for these sensors. When the shock waves move toward the intake entrance and the intake mass flow rate increases, several compression waves move from the intake entrance to its end and will increase the static pressure inside the intake. These compression waves increase the static pressure of sensors S18 and S23; however, for a short time, the number of compression waves that have passed over S18 are more than those passed over sensor S23, and as a result, the static pressure of the sensor S18 is greater than that of S23 up to $t = 56.0$ ms. Once the waves are reflected from face of the plug, they first pass through sensor S23, and as a result, the corresponding static pressure read from sensor 23 is greater than the one measured by the S18 sensor, which happens after $t = 56.0$ ms.

As the outside shock waves approach the intake entrance and the separation region reduces, the lambda shock wave becomes nearly a normal shock. The normal shock is weakened when it approaches the throat section. A small separation region behind this shock reduces the flow area, and as a result, the Mach number at the position of sensor T6 becomes unity for $t = 57.3$ ms, as seen from Fig. 14. At $t = 57.5$ ms, the flow over sensor T6 becomes supersonic. A weak normal shock wave forms at the intake entrance and starts to move downstream. This shock is weak, and a small separation region behind it reduces the effective area of the flow. Therefore, only a

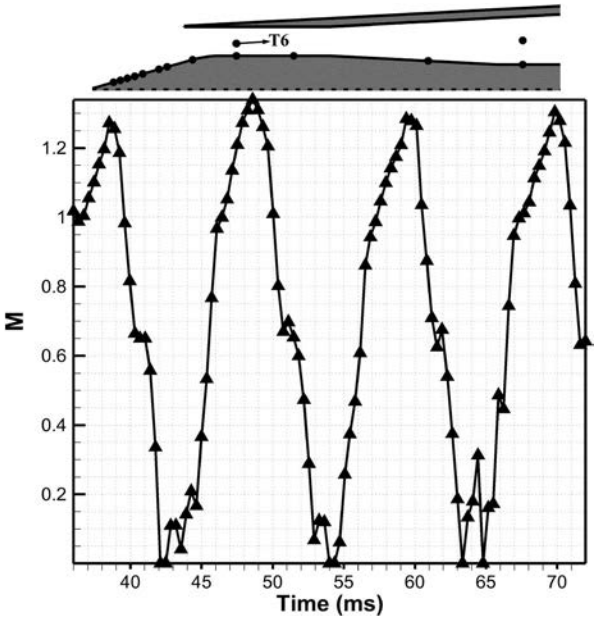

Fig. 14 Mach number variation measured by sensor T6 for $M\infty = 2.0$ and EBR = 70.0%.

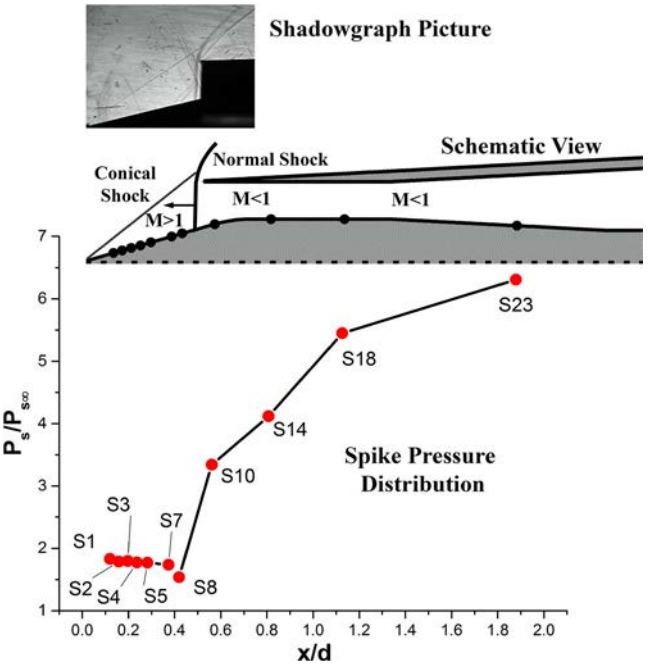

Fig. 15 Flow characteristics at $t = 50.0$ ms.

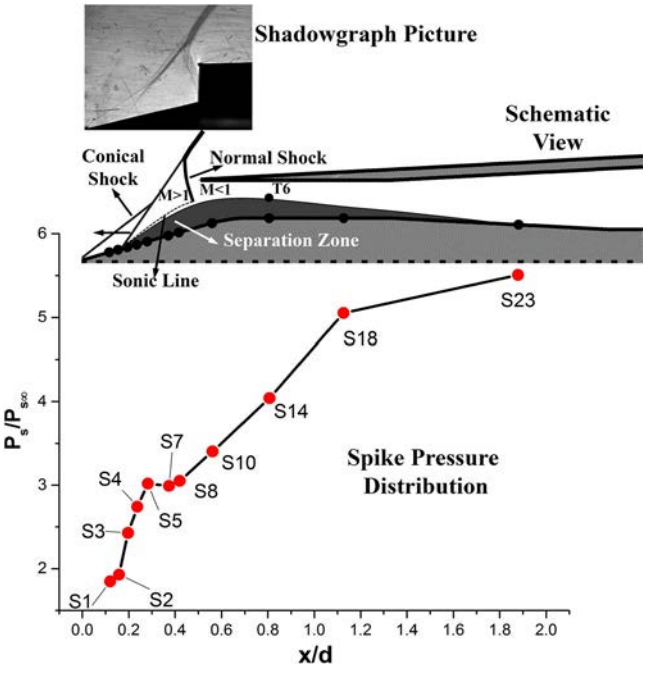

Fig. 16 Flow characteristics at $t = 52.0$ ms.

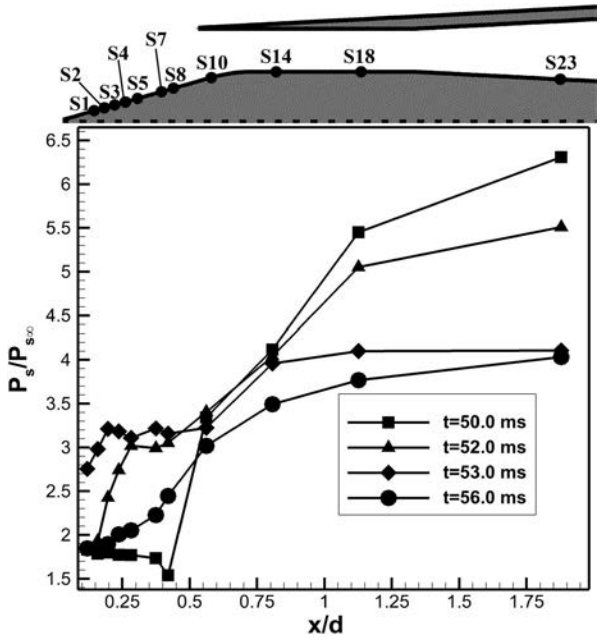

Fig. 17 Static pressure variations over the spike surface at different instances for $M_\infty = 2.0$ and EBR = 70.0%.

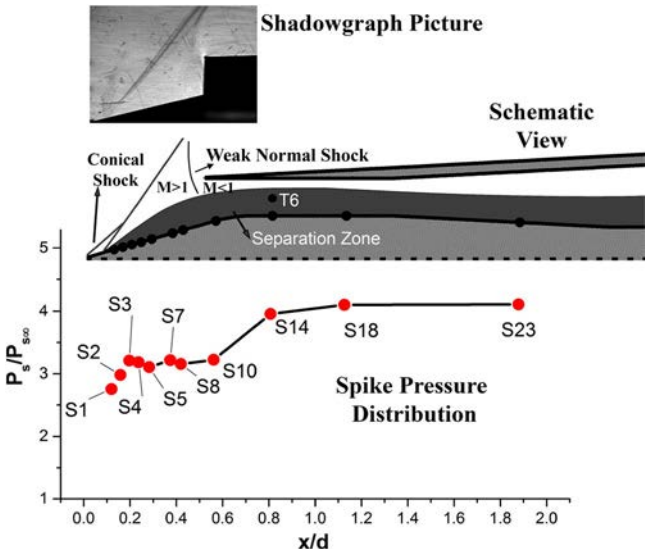

Fig. 18 Flow characteristics at $t = 53.0$ ms.

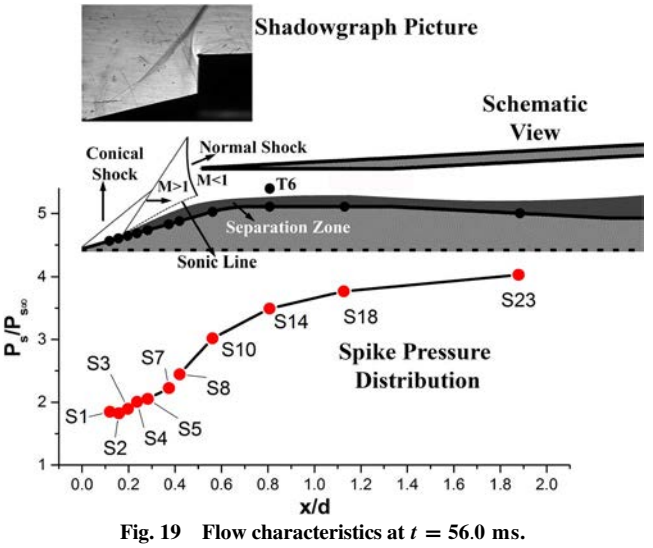

Fig. 19 Flow characteristics at $t = 56.0$ ms.

small subsonic region forms behind this normal shock. The approximate sonic line is shown in Fig. 21. The supersonic flow in the throat section accelerates when it reaches the subsonic diffuser where the flow area increases; thus, the Mach number increases too. The supersonic flow inside the subsonic diffuser encounters a high backpressure, and a normal shock between sensors S18 and S23 forms. The pressure jump between these sensors according to the spike pressure distribution shown in Fig. 21 and at $t = 57.5$ ms in Fig. 20 confirms the presence of a normal shock inside the intake. At this condition, in spite of the value of EBR that corresponds to the subcritical operating condition, for a short time the intake becomes supercritical. This subject has been already specified in Fig. 13.

Figure 20 further shows that a large difference between the pressures sensed by sensors S18 and S23 exists from $t = 57.5$ ms to $t = 58.5$ ms. This indicates that the normal shock is moving downstream. When this moving normal shock enters a larger duct area, its upstream Mach number increases, which will strengthen it. However, as the intake mass flow rate is increased, the static pressure

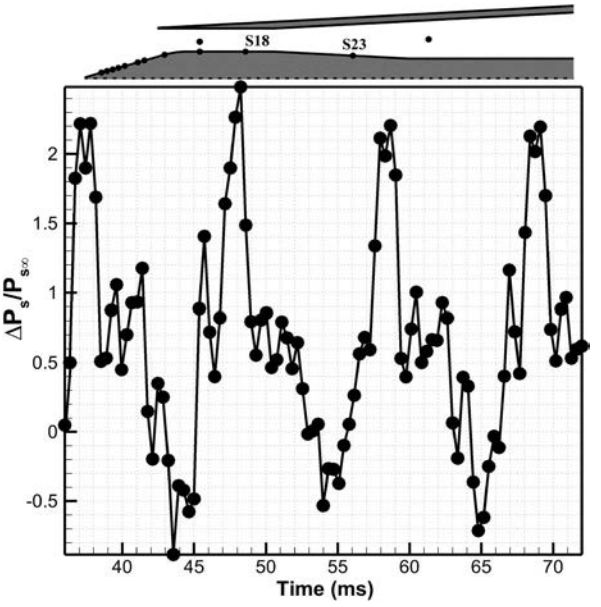

Fig. 20 Difference of static pressure ratio measured by sensors S18 and S23 $[(P_{sS23} - P_{sS18})/P_{s\infty}]$.

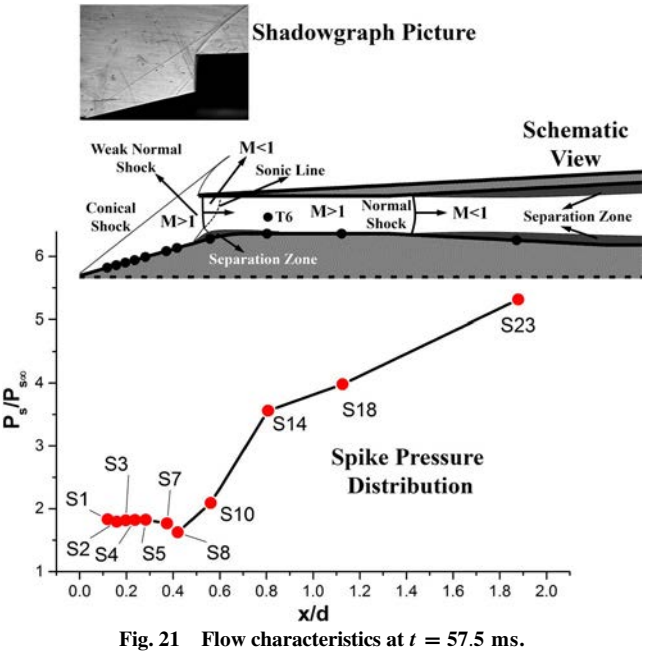

Fig. 21 Flow characteristics at $t = 57.5$ ms.

inside the intake increases, too, which will cause a large backpressure at the end of the intake. This increased backpressure will in turn reverse the direction of motion of the inside normal shock.

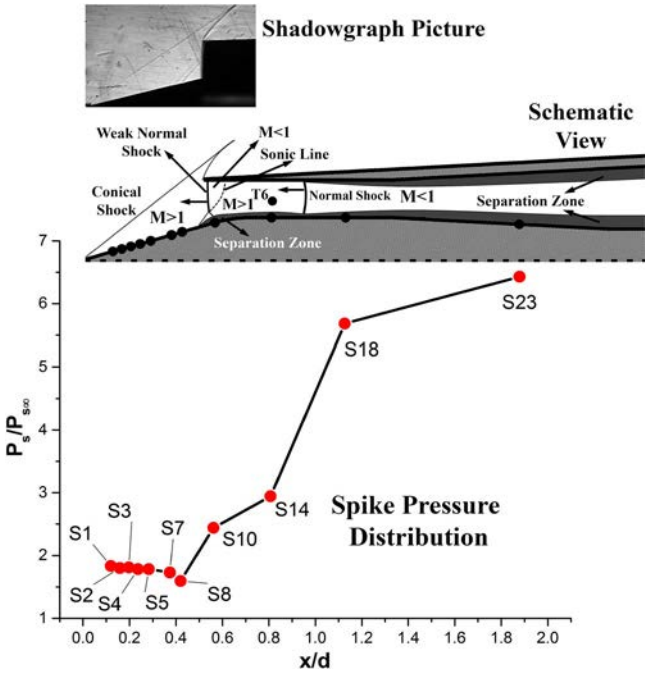

Fig. 22 Flow characteristics at $t = 60.0$ ms.

Furthermore, Fig. 13 shows that, at $t = 59.0$ ms, sensor S10 shows its lowest static pressure; therefore, the entrance normal shock must be located after this sensor. However, a jump in the output of sensor S10 after 1 ms, about $t = 60.0$ ms, is seen, which may indicate that the entrance normal shock does not move inside the intake very far and it moves upstream very soon. The output of sensor S10 starts increasing at $t = 59.8$ ms, showing an increase in the static pressure in that region, as seen from Fig. 13, whereas at this time, the Mach number measured by sensor T6 is supersonic, $M = 1.28$, according to Fig. 14. This means that the entrance normal shock starts moving upstream before the internal normal shock reaches it. The mechanism that pushes the entrance normal shock upstream, backward, is the increase in the static pressure downstream of the internal normal shock that propagates upstream through the thickened boundary layer behind the intake shocks.

The Mach number measured by the sensor T6 becomes sonic at $t = 60.5$ ms, and it then becomes subsonic. Thus, at $t = 60.0$ ms, as seen from Fig. 22, the internal normal shock is located between sensors T6 (S14) and S18. According to this figure, the separated flow over the spike surface causes propagation of acoustic pressure waves upstream and pushes the entrance normal shock toward the spike tip. In addition, the spike pressure distribution at $t = 60.0$ ms (Fig. 22) clearly indicates the presence of a normal shock wave located between sensors S14 and S18.

At $t = 60.5$ ms, the pressure measured by the sensor S10 is similar to the one measured at the beginning of the buzz cycle ($t = 50.0$ ms), as seen from Fig. 13. The entrance normal shock that is now outside the intake is moving upstream, and the static pressure behind it increases. The internal normal shock, which is also moving upstream, disappears when it reaches the subsonic region formed behind the outside normal shock. This subject can be confirmed from observing the static pressure distribution over the spike at $t = 50.0$ ms, shown

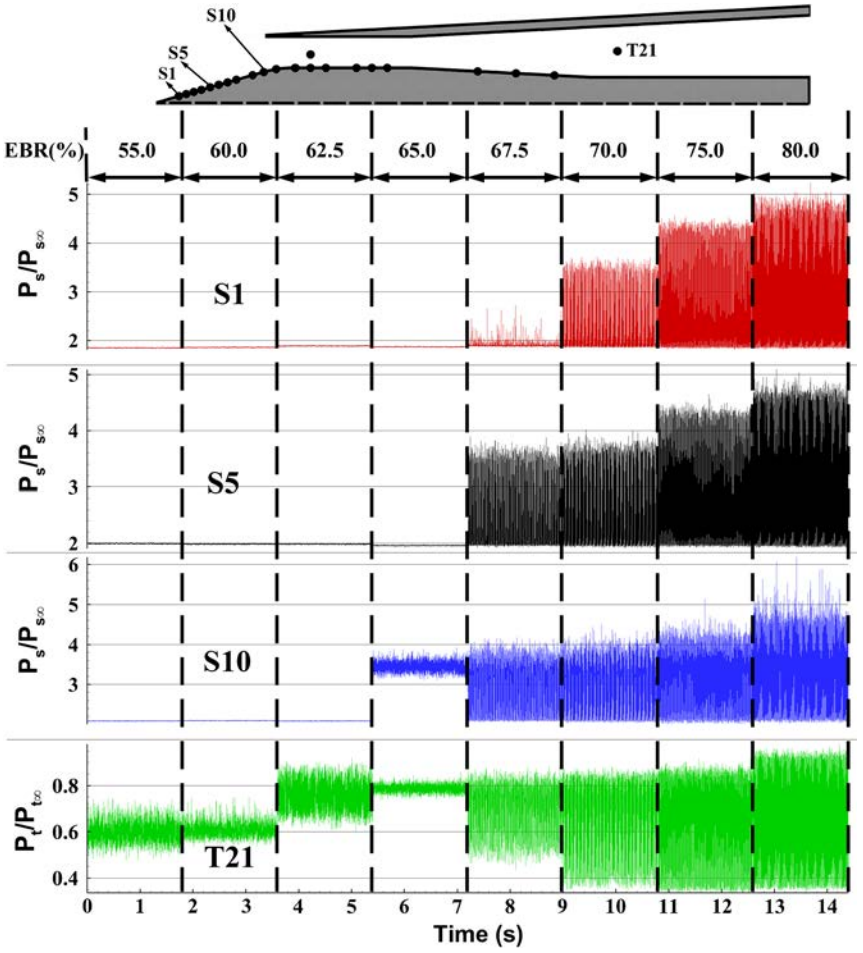

Fig. 23 Pressure recordings measured by sensors S1, S5, S10, and T21 for $M\infty = 2.2$.

in Fig. 15. In addition, the subsonic Mach number at the throat section measured by sensor T6 and shown in Fig. 14 after $t = 60.5$ ms further confirms the previous statement.

E. Buzz Onset for M_∞ Equal to 2.2

The pressure signals obtained from sensors S1, S5, S10, and T21 for $M_\infty = 2.2$ and for various EBRs are shown in Fig. 23. According to this figure, the operating condition of the intake is subcritical for EBR = 65.0%, whereas the first subcritical EBR for $M_\infty = 1.8$ and $M_\infty = 2.0$ was for EBR = 62.5%. When the freestream Mach number is increased, the intake shock waves become stronger, and they stand farther downstream. As a result, the internal normal shock is expelled from the intake at higher EBR. In addition, Fig. 23 shows that the buzz has been started when EBR = 67.5%. For this EBR, sensor S1 is at the edge of the buzz oscillations and senses only some of the fluctuations. However, for EBR = 70.0%, this sensor is positioned completely inside the buzz fluctuation region.

Shadowgraph pictures show very small-amplitude oscillations, which are local for EBR = 65.0%. However, spectra of the pressure signals do not reveal any dominant frequency except for sensor S8, which is just behind the oscillatory shock wave, shown in Fig. 24. This behavior has already been observed for lower Mach numbers examined in this study. According to Fig. 24, the frequency of the oscillation is 96.0 Hz. Using Eq. (2), it is found that the frequency of the first mode of acoustic resonance is 94.0 Hz, which is very close to the aforementioned observed frequency. Thus, again it can be concluded that acoustic resonance inside the intake duct can cause local fluctuations for the outer shock waves. This subject can affect designing the intake geometry because the acoustic resonance frequency is a function of the intake geometry according to Eq. (2).

As seen from Fig. 25, the buzz frequencies for EBRs of 67.5, 70.0, 75.0, and 80.0% are 80.0, 85.0, 104.0, and 120.0 Hz, respectively. Comparison of these frequencies with frequencies of various modes of the acoustic resonance shows that these frequencies are not congruent with the acoustic frequencies. Surveying the shadowgraph pictures indicates that the amplitudes of the buzz fluctuations for these EBRs are altogether large. Thus, little buzz does not happen for this freestream Mach number and for all EBRs that were examined in this study. Furthermore, investigation of the buzz cycle for this Mach number shows that the sequence of physical phenomena of the buzz cycle is very similar to those explained for $M_\infty = 2.0$.

F. Effects of Mach Number

As seen from the previous discussions, for $M_\infty = 1.8$ and $M_\infty = 2.0$, the subcritical operating condition is obtained for EBR $\geq$ 62.5%, and for $M_\infty = 2.2$, it is obtained for EBR $\geq$ 65.0%. For higher freestream Mach numbers, the intake shocks become stronger and stand at a location far downstream. Therefore, a higher value of EBR is needed to expel out the internal normal shock out of the intake.

The buzz onset is occurred at EBR = 67.5% for $M_\infty = 1.8$, whereas for $M_\infty = 2.0$ and $M_\infty = 2.2$, it is initiated at EBR = 67.5%. Variation of the buzz dominant frequency versus EBR is shown in Fig. 26. As seen, the buzz frequency increases when EBR increases, and it decreases as the freestream Mach number is increased. When EBR increases, the intake shocks stand at a location far upstream over the spike, and when the freestream Mach number increases, they stand at a position far downstream. According to the Dailey criterion and the buzz description for $M_\infty = 2.0$ in this paper, the region of flow separation behind the intake shocks increases when the shocks stand at a location far upstream over the spike. As a result, the conditions leading to the buzz oscillations according to the Dailey criterion are formed in a short time and results in a decrease of the buzz frequency. The reason for the high frequency obtained for $M_\infty = 1.8$ and EBR = 80% as seen from Fig. 26 has been previously described.

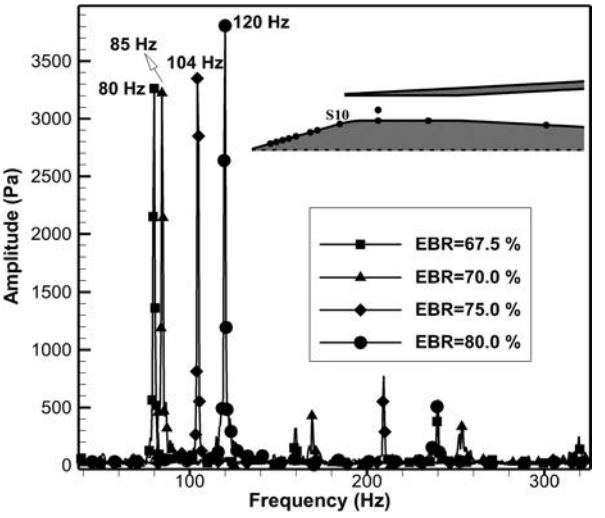

Fig. 25 Spectra of pressure signals obtained from sensor S10 for $M_\infty = 2.2$ and various EBRs.

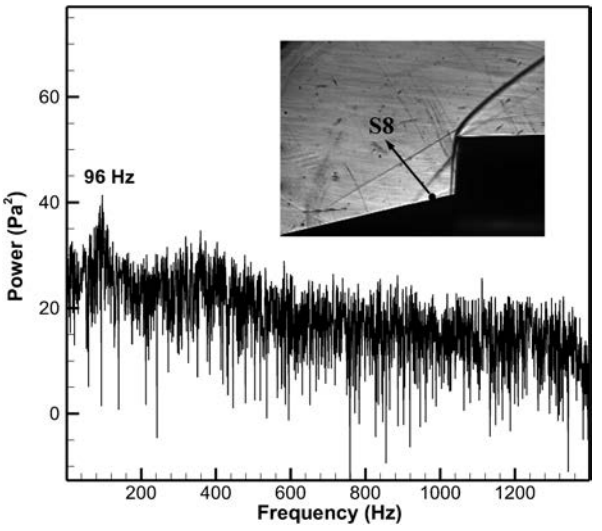

Fig. 24 Spectrum of pressure signal measured from sensor S8 for $M_\infty = 2.2$ and EBR = 65.0%.

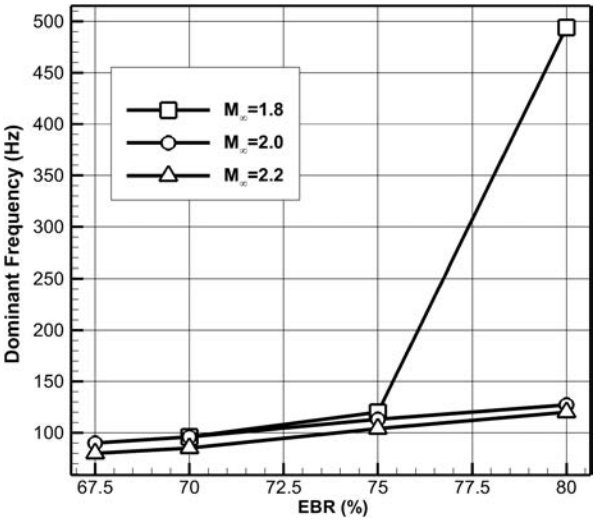

Fig. 26 Dominant frequencies of the buzz oscillations for each freestream Mach number.

IV. Conclusions

The buzz cycle in a mixed-compression supersonic intake has been extensively studied from the experimental data. Both static and total pressures were recorded by high-frequency and high-accuracy pressure transducers. In addition, shadowgraph pictures were used to describe the buzz onset and the buzz cycle for all freestream Mach numbers $M_\infty = 1.8$, 2.0, and 2.2, and for 0 deg angle of attack. Results demonstrate that the acoustic characteristics of the intake duct have a strong effect on the buzz triggering phenomenon. Acoustic resonance causes local fluctuations before the buzz onset, and they are amplified with the same frequency when the buzz starts. Little buzz does not take place in the current intake for the examined exit blockage ratios except for $M_\infty = 1.8$ when the exit blockage ratio is 70.0%. Large flow separation in some instants of the buzz cycle leads to the formation of large-amplitude buzz oscillations with large frequencies, which has rarely been observed previously. These fluctuations have characteristics of both little buzz (Ferri-type instabilities) and big buzz (Dailey-type instabilities). When exit blockage ratio is increased, both amplitude and frequency of the buzz oscillations increases. Investigation of the buzz cycle shows that interaction of the shock waves with the boundary layer, which causes the flow separation behind the shock waves as well as the acoustic compression waves, have important roles in the establishment of the buzz fluctuations. The buzz frequency is decreased when the freestream Mach number is increased.

References

[1] Seddon, J., and Goldsmith, E. L., *Intake Aerodynamics*, Collins, London, 1985, Chaps. 1, 10, 15.

[2] Oswatitsch, K., "Pressure Recovery in Missile in Reaction Propulsion at High Supersonic Speeds," NACA TM-1140, 1947.

[3] Hill, P. G., and Peterson, C. R., *Mechanics and Thermodynamics of Propulsion*, 2nd ed., Addison Wesley, New York, 1992, Chap. 6.

[4] Hankey, W. L., and Shang, S. J., "Analysis of Self-Excited Oscillations in Fluid Flows," *13th Fluid and PlasmaDynamics Conference*, AIAA Paper 1980-1346, 1980.

[5] Ferri, A., and Nucci, L. M., "The Origin of Aerodynamic Instability of Supersonic Inlet at Subcritical Condition," NACA RM-L50K30, 1951.

[6] Dailey, C. L., "Supersonic Diffuser Instability," Ph.D. Dissertation, California Inst. of Technology, Pasadena, CA, 1954.

[7] Fisher, S. A., Neale, M. C., and Brooks, A. J., "On the Subcritical Stability of Variable Ramp Intakes at Mach Number Around 2.0," National Gas Turbine Establishment Rept. ARC-R/M-3711, Fleet, England, U.K., 1970.

[8] Trapier, S., Duveau, P., and Deck, S., "Experimental Study of Supersonic Inlet Buzz," *AIAA Journal*, Vol. 53, No. 12, 2006, pp. 2354–2365. doi:10.2514/1.20451

[9] Newsome, R. W., "Numerical Simulation of Near-Critical and Unsteady, Subcritical Inlet Flow," *AIAA Journal*, Vol. 22, No. 12, 1984, pp. 1375–1379. doi:10.2514/3.48577

[10] Sterbentz, W. H., and Davids, J., "Amplitude of Supersonic Diffuser Flow Pulsations," NACA RM-E52I24, 1952.

[11] Sterbentz, W. H., and Evvard, J. C., "Criterions for Prediction and Control of Ram-Jet Flow Pulsations," NACA TN-3506, 1955.

[12] Trimpi, R. L., "A Theory for Stability and Buzz Pulsation Amplitude in Ram Jets and an Experimental Investigation Including Scale Effects," NACA Rept. 1265, 1956.

[13] Nagashima, T., Obokata, T., and Asanuma, T., "Experiment of Supersonic Air Intake Buzz," Inst. of Space and Aeronautical Science Rept. 481, Tokyo, 1972.

[14] Bogar, T. J., Sajben, M., and Kroutil, J. C., "Characteristic Frequencies in Transonic Diffuser Flow Oscillations," *AIAA Journal*, Vol. 21, No. 9, 1983, pp. 1232–1240. doi:10.2514/3.8234

[15] Park, I., Ananthkrishnan, N., Tahk, M., Vineeth, C. R., and Gupta, N. K., "Low-Order Model for Buzz Oscillations in the Intake of a Ramjet Engine," *Journal of Propulsion and Power*, Vol. 27, No. 2, 2011, pp. 503–506. doi:10.2514/1.50093

[16] Shi, X., Chang, J., Bao, W., Yu, D., and Li, B., "Supersonic Inlet Buzz Margin Control of Ducted Rockets," *Proceedings of the Institution of Mechanical Engineers, Part G: Journal of Aerospace Engineering*, Vol. 224, No. 12, 2011, pp. 1131–1139. doi:10.1243/09544100JAERO687

[17] Lu, P., and Jain, L., "Numerical Investigation of Inlet Buzz Flow," *Journal of Propulsion and Power*, Vol. 14, No. 1, 1998, pp. 90–100. doi:10.2514/2.5254

[18] Trapier, S., Deck, S., and Duveau, P., "Delayed Detached-Eddy Simulation and Analysis of Supersonic Inlet Buzz," *AIAA Journal*, Vol. 46, No. 1, 2008, pp. 118–131. doi:10.2514/1.32187

[19] Namkoung, H. J., Hong, W., Kim, J. M., Yi, J., and Kim, C., "Effects of Angles of Attack and Throttling Conditions on Supersonic Inlet Buzz," *International Journal of Aeronautical and Space Sciences*, Vol. 13, No. 3, 2012, pp. 296–306. doi:10.5139/IJASS.2012.13.3.296

[20] Fujiwara, H., Murakami, A., and Watanabe, Y., "Numerical Analysis on Shock Oscillation of Two-Dimensional External Compression Intakes," *32nd AIAA Fluid Dynamics Conference and Exhibit*, AIAA Paper 2002-2740, June 2002.

[21] Vivek, P., and Mittal, S., "Buzz Instability in a Mixed-Compression Air Intake," *Journal of Propulsion and Power*, Vol. 25, No. 3, 2009, pp. 819–822. doi:10.2514/1.39751

[22] Yeom, H. W., Kim, S. J., Sung, H. G., and Yang, V., "Inlet Buzz and Combustion Oscillation in an Axisymmetric Ramjet Engine," *48th AIAA Aerospace Sciences Meeting*, AIAA Paper 2010-0756, Jan. 2010.

[23] Lee, H. J., Lee, B. J., Kim, S. D., and Jeung, I., "Flow Characteristics of Small-Sized Supersonic Inlets," *Journal of Propulsion and Power*, Vol. 27, No. 2, 2011, pp. 306–318. doi:10.2514/1.46101

[24] Kwak, E., and Lee, S., "Convergence Study of Inlet Buzz Frequency with Computational Parameters," *29th AIAA Applied Aerodynamics Conference*, AIAA Paper 2011-3362, June 2011.

[25] Nakayama, T., Sato, T., Akatsuka, M., Hashimoto, A., Kojima, T., and Taguchi, H., "Investigation on Shock Oscillation Phenomenon in a Supersonic Air Inlet," *41st AIAA Fluid Dynamics Conf. and Exhibit*, AIAA Paper 2011-3094, June 2011.

[26] Hong, W., and Kim, C., "Numerical Study on Supersonic Inlet Buzz Under Various Throttling Conditions and Fluid-Structure Interaction," *29th AIAA Applied Aerodynamics Conference*, AIAA Paper 2011-3967, June 2011.

[27] Chima, R. V., "Analysis of Buzz in a Supersonic Inlet," NASA TM-2012-217612, 2012.

[28] Kim, S. J., Yeom, H. W., Sung, H. G., and Yang, V., "Inlet Buzz and Combustion Oscillation in a Liquid-Fueled Ramjet Engine," *49th AIAA Aerospace Sciences*, AIAA Paper 2011-0230, Jan. 2011.

[29] Nishizawa, U., Kameda, M., and Watanabe, Y., "Computational Simulation of Shock Oscillation Around a Supersonic Air-Intake," *36th AIAA Fluid Dynamics Conference and Exhibit*, AIAA Paper 2006-3042, June 2006.

[30] Kotteda, V. M. K., and Mittal, S., "Viscous Flow in a Mixed Compression Intake," *International Journal for Numerical Methods in Fluids*, Vol. 67, No. 11, 2011, pp. 1393–1417. doi:10.1002/fld.v67.11

[31] Herges, T. G., Dutton, J. C., and Elliott, G. S., "High-Speed Schlieren Analysis of Buzz in a Relaxed-Compression Supersonic Inlet," *48th AIAA/ASME/SAE/ASEE Joint Propulsion Conference and Exhibit*, AIAA Paper 2012-4146, July–Aug. 2012.

[32] Tindell, R. H., "Inlet Drag and Stability Considerations for $M_o = 2.00$ Design," *Journal of Aircraft*, Vol. 18, No. 11, 1981, pp. 943–950. doi:10.2514/3.57584

[33] Hongprapas, S., Kozak, J. D., Moses, B., and Ng, W. F., "A Small Scale Experiment for Investigating the Stability of a Supersonic Inlet," *35th Aerospace Sciences Meeting and Exhibit*, AIAA Paper 1997-0611, Jan. 1997.

[34] Tan, H., Sun, S., and Yin, Z., "Oscillatory Flows of Rectangular Hypersonic Inlet Unstart Caused by Downstream Mass-Flow Choking," *Journal of Propulsion and Power*, Vol. 25, No. 1, 2009, pp. 138–147. doi:10.2514/1.37914

[35] Chang, J., Wang, L., Bao, W., Qin, J., Niu, J., and Xue, W., "Novel Oscillatory Patterns of Hypersonic Inlet Buzz," *Journal of Propulsion and Power*, Vol. 28, No. 6, 2012, pp. 1214–1221. doi:10.2514/1.B34553

[36] Trapier, S., Deck, S., and Duveau, P., "Time-Frequency Analysis and Detection of Supersonic Inlet Buzz," *AIAA Journal*, Vol. 45, No. 9, 2007, pp. 2273–2284. doi:10.2514/1.29196

[37] Herrmann, D., and Triesch, K., "Experimental Investigation of Isolated Inlets for High Agile Missiles," *Aerospace Science and Technology*, Vol. 10, No. 8, 2006, pp. 659–667. doi:10.1016/j.ast.2006.05.004

[38] Hirschen, C., Herrmann, D., and Gülhan, A., "Experimental Investigations of the Performance and Unsteady Behaviour of a Supersonic Intake," *Journal of Propulsion and Power*, Vol. 23, No. 3, 2007, pp. 566–574.
doi:10.2514/1.25103

[39] Herrmann, D., Triesch, K., and Gülhan, A., "Experimental Study of Chin Intakes for Airbreathing Missiles with High Agility," *Journal of Propulsion and Power*, Vol. 24, No. 2, 2008, pp. 236–244.
doi:10.2514/1.29672

[40] Herrmann, D., Blem, S., and Gülhan, A., "Experimental Study of Boundary-Layer Bleed Impact on Ramjet Inlet Performance," *Journal of Propulsion and Power*, Vol. 27, No. 6, 2011, pp. 1186–1195.
doi:10.2514/1.B34223

[41] Herrmann, D., Siebe, F., and Gülhan, A., "Pressure Fluctuations (Buzzing) and Inlet Performance of an Airbreathing Missile," *Journal of Propulsion and Power*, Vol. 29, No. 4, 2013, pp. 839–848.
doi:10.2514/1.B34629

[42] Soltani, M. R., Farahani, M., and Asgari Kaji, M. H., "An Experimental Study of Buzz Instability in an Axisymmetric Supersonic Inlet," *Scientia Iranica*, Vol. 18, No. 2, 2011, pp. 241–249.
doi:10.1016/j.scient.2011.03.019

[43] Soltani, M. R., and Farahani, M., "Experimental Investigation of Effects of Mach Number on the Flow Instability in a Supersonic Inlet," *Experimental Techniques*, Vol. 37, No. 3, 2013, pp. 46–54.
doi:10.1111/ext.2013.37.issue-3

[44] Soltani, M. R., and Farahani, M., "Effects of Angle of Attack on the Inlet Buzz," *Journal of Propulsion and Power*, Vol. 28, No. 4, 2012, pp. 747–757.
doi:10.2514/1.B34209

[45] Soltani, M. R., and Farahani, M., "Performance Study of an Inlet in Supersonic Flow," *Proceedings of the Institution of Mechanical Engineers, Part G: Journal of Aerospace Engineering*, Vol. 227, No. 1, 2012, pp. 159–174.
doi:10.1177/0954410011426672

[46] Soltani, M. R., Sepahi Younsi, J., and Daliri, A., "Performance Investigation of a Supersonic Air Intake in the Presence of the Boundary Layer Suction," *Proceedings of the Institution of Mechanical Engineers, Part G: Journal of Aerospace Engineering*, Vol. 229, No. 8, 2015, pp. 1495–1509.
doi:10.1177/0954410014554815

[47] Soltani, M. R., Sepahi Younsi, J., and Farahani, M., "Effects of the Boundary-Layer Bleed Parameters on the Supersonic Intake Performance," *Journal of Propulsion and Power*, Vol. 31, No. 3, 2015, pp. 826–836.
doi:10.2514/1.B35461

F. Alvi
Associate Editor